The Astrophysical Journal, 888:11 (9pp), 2020 January 1 https://doi.org/10.3847/1538-4357/ab54c9

PIC Simulation of a Shock Tube: Implications for Wave Transmission in the Heliospheric Boundary Region

S. Matsukiyo[1], T. Noumi[1], G. P. Zank[2], H. Washimi[2], and T. Hada[1]
[1] Faculty of Engineering Sciences, Kyushu University, Kasuga, Fukuoka, 816-8580, Japan; matsukiy@esst.kyushu-u.ac.jp, nomi@esst.kyushu-u.ac.jp, hada@esst.kyushu-u.ac.jp
[2] Center for Space Plasma and Aeronomie Research (CSPAR), University of Alabama in Huntsville, Huntsville, AL 35805, USA; garyp.zank@gmail.com, hwashimi2004@hotmail.com
Received 2019 June 16; revised 2019 November 2; accepted 2019 November 4; published 2019 December 27

Abstract

A shock tube problem is solved numerically by using one-dimensional full particle-in-cell simulations under the condition that a relatively tenuous and weakly magnetized plasma is continuously pushed by a relatively dense and strongly magnetized plasma having supersonic relative velocity. A forward and a reverse shock and a contact discontinuity are self-consistently reproduced. The spatial width of the contact discontinuity increases as the angle between the discontinuity normal and ambient magnetic field decreases. The inner structure of the discontinuity shows different profiles between magnetic field and plasma density, or pressure, which is caused by a non-MHD effect of the local plasma. The region between the two shocks is turbulent. The fluctuations in the relatively dense plasma are compressible and propagating away from the contact discontinuity, although the fluctuations in the relatively tenuous plasma contain both compressible and incompressible components. The source of the compressible fluctuations in the relatively dense plasma is in the relatively tenuous plasma. Only compressible fast mode fluctuations generated in the relatively tenuous plasma are transmitted through the contact discontinuity and propagate in the relatively dense plasma. These fast mode fluctuations are steepened when passing the contact discontinuity. This wave steepening and probably other effects may cause the broadening of the wave spectrum in the very local interstellar medium plasma. The results are discussed in the context of the heliospheric boundary region or heliopause.

Unified Astronomy Thesaurus concepts: Space plasmas (1544); Heliosphere (711); Solar transition region (1532); Interstellar magnetic fields (845); Interplanetary magnetic fields (824)

1. Introduction

The heliospheric boundary region plays very important roles in the transport, conversion, and exchange of energy and matter between the heliosphere and interstellar space. The region has been explored in situ by the *Voyager* spacecraft. *Voyager 1* crossed the termination shock of the solar wind (SW) in 2004 (Burlaga et al. 2005; Decker et al. 2005; Gurnett & Kurth 2005; Stone et al. 2005) and heliopause in 2012 (Burlaga et al. 2013; Gurnett et al. 2013; Krimigis et al. 2013; Stone et al. 2013), and has since traveled in the very local interstellar medium (VLISM). *Voyager 2* crossed the termination shock in 2007 (Burlaga et al. 2008; Decker et al. 2008; Gurnett & Kurth 2008; Richardson et al. 2008; Stone et al. 2008), and it recently crossed the heliopause in 2018. The heliopause is a contact discontinuity that separates the SW plasma and the interstellar plasma from the perspective of magnetohydrodynamics (MHD).

There are a number of unresolved issues regarding the structure of the boundary region since it appears to depart from what is expected from simple MHD theory. It is well known, for instance, that the behavior of the magnetic field and cosmic-ray particles in the heliopause transition region observed by *Voyager 1* is not well correlated (Burlaga & Ness 2014). Since the *Voyager* spacecraft have explored the boundary region along only two radial paths, the detailed structure of the region has been studied by using numerical simulations. In particular kinetic scale structures are discussed using hybrid and full particle-in-cell (PIC) simulations. Hybrid simulations of the termination shock were presented by many authors (Liewer & Goldstein 1993; Kucharek & Scholer 1995; Liewer et al. 1995; Lipatov et al. 1998; Lipatov & Zank 1999; Wu et al. 2009, 2010; Giacalone & Burgess 2010; Giacalone & Decker 2010; Liu et al. 2010) focusing on ion kinetic effects, while PIC simulations were used to address both ion and electron dynamics at the heliospheric termination shock (Lee et al. 2005; Matsukiyo et al. 2007; Matsukiyo & Scholer 2011, 2014; Oka et al. 2011; Yang et al. 2015; Lembege & Yang 2018). Kinetic simulations of the region beyond the termination shock such as heliosheath, heliopause, etc., have also been undertaken, although not so extensively. Magnetic reconnection in the inner heliosheath is discussed using hybrid simulations (Burgess et al. 2016) and PIC simulations (Drake et al. 2017). The stability of the pickup ion distribution function has been examined for various kinetic instabilities by using hybrid (Florinski et al. 2010, 2016; Liu et al. 2012; Min & Liu 2018) and PIC (Niemiec et al. 2016) simulations.

Because kinetic numerical simulations are very costly, they are usually used to reproduce a local structure. However, there are some phenomena for which a nonlocal effect is expected to be essential. Burlaga et al. (2015, 2018a) showed that *Voyager 1* observed compressible weak magnetic fluctuations in the VLISM immediately outside the heliopause even during a period during which there were no large SW disturbances, and they discussed the possibility that the fluctuations are generated in the inner heliosheath and passed across the heliopause. This idea is supported theoretically by Zank et al. (2017). In order to reproduce a nonlocal effect in a numerical simulation, a large system size is necessary in at least one appropriate direction. In this study we investigate the radial structure of a boundary region including a shock and a contact discontinuity as in the

heliospheric boundary region with a termination shock and heliopause, by using a one-dimensional PIC simulation. Kinetic properties at the boundary of two plasmas in contact with each other, i.e., at a contact discontinuity, are investigated including mixing and the radial nonlocal effect of wave propagation. To mimic the heliospheric boundary region, we numerically solve the so-called shock tube problem. As explained in the next section, it reproduces the evolution of a system that includes three discontinuities, a forward and a reverse shock and a contact discontinuity.

The paper is organized as follows. In Section 2, simulation settings and parameters are presented. The results of the simulations are discussed in Section 3. Then, the summary and discussion are given in Section 4.

2. Simulation Settings

The shock tube problem is solved numerically using a one-dimensional PIC code. Initially, the system is divided into two regions. The region with $X > X_0$ is filled with a relatively tenuous and weakly magnetized plasma at rest, while the region with $X < X_0$ is filled with a relatively dense and strongly magnetized plasma flowing with constant bulk velocity. The left boundary at $X = 0$ is open and fresh dense plasma is injected continuously. At the right boundary ($X = L$), the plasma is reflected and electromagnetic fields are absorbed. The distribution functions of both plasmas are assumed to be (shifted) Maxwellians. With the above initial conditions, three discontinuities are self-consistently produced as time passes propagating from left to right. The rightmost one is a forward shock, the leftmost one a reverse shock, and the middle one is a contact discontinuity, respectively.

The simulation parameters are as follows. The plasma density from the left to the right is 9, the relative temperature is 4, and the relative strength of tangential magnetic field is 6, respectively. The ion to electron mass ratio is $m_i/m_e = 25$ in both plasmas. Although this mass ratio is unrealistically small, electron and ion phenomena are sufficiently well separated to qualitatively resolve the corresponding structures. We confirmed that the structures of electromagnetic fields as well as particle phase space distributions are essentially unchanged when the mass ratio is increased to 100 for Run 3 below (not shown). In the left plasma, the ratio of electron plasma to cyclotron frequencies is 2.37 and plasma beta is 0.225, and the temperature is identical for both electrons and ions. While the above parameters are fixed, we perform five runs with different angles $\Theta_{\rm Bn}$ of ambient magnetic field with respect to the X-axis in the X–Z plane. The above relative values of density, temperature, and magnetic field strength are qualitatively similar to those between the local interstellar medium (LISM) and SW. Therefore, the left plasma mimics the local interstellar medium, while the right plasma mimics the SW plasma. In this context the forward and reverse shocks correspond to the SW termination shock and the bow shock in the LISM, and the contact discontinuity to the heliopause, respectively. Hereafter, we refer to the left plasma as interstellar (IS) plasma and the right plasma as SW plasma for convenience.

The system size is $L = 506c/\omega_{\rm pi,SW}$ and is divided into 80,000 grid points. Here, c is the speed of light, $\omega_{\rm pi,SW}$ denotes the ion plasma frequency in the SW, and the grid size is a little smaller than the SW Debye length, $\Delta X = 0.63\lambda_{\rm De,SW}$. We recognize that the system size is too small to compare the results with the observations quantitatively, even when limiting our discussions to essentially one-dimensional phenomena. Nonetheless, the simulations serve to illustrate what we regard as the underlying essential physical phenomena that are qualitatively important in the boundary region. We emphasize that the system size treated here is not large in the sense of the global heliospheric structure and therefore represents a small 1D spatial "slice" of the actual heliosphere. We do not presume to address the global physics of the heliosphere in this paper, since the question of what wave fluctuations will be transmitted across the heliosheath has to be addressed on kinetic scales corresponding to these fluctuations. Accordingly, a coarsely resolved global simulation cannot be used to investigate the transmission of short wavelength fluctuations across the heliopause. For this reason, we focus on a spatially 1D simulation.

Table 1
Simulation Parameters

Run	1	2	3	4	5
$\Theta_{\rm Bn,IS}$	90.0	87.5	85.0	82.5	80.0
$\Theta_{\rm Bn,SW}$	90.0	75.3	62.3	51.7	43.4
$\beta_{\rm IS}$	0.225	0.225	0.223	0.221	0.218
$\beta_{\rm SW}$	0.225	0.211	0.178	0.141	0.109
$\omega_{\rm pe,IS}/\Omega_{e,\rm IS}$	2.37	2.37	2.36	2.35	2.34
$\omega_{\rm pe,SW}/\Omega_{e,\rm SW}$	4.74	4.59	4.22	3.75	3.31
$M_{\rm A,BS}$	1.2	1.2	1.2	1.2	1.2
$M_{\rm A,TS}$	6.5	6.1	5.6	4.5	4.0

We note also that other aspects underpinning the physics of the large-scale global heliospheric interaction with the local interstellar medium are not important to the specific problem of compressible wave generation in the VLISM. For example, the effect of collisions will not change the results discussed below. For charge exchange collisions, the inner heliosheath, the neutral H-proton charge exchange mean free path is ~1000 au, and in the VLISM, neutral H-proton charge exchange mean free path is ~60 au. Therefore, for the kinetic scales of interest in this paper, charge exchange is irrelevant. Non-charge exchange collisionality of the VLISM has been recognized recently as an interesting further aspect of the physics (Mostafavi & Zank 2018). However, the collisional length scale of proton–proton collisions, for example, is 0.3 au, meaning that on rather larger scales, the VLISM can be regarded as collisional. On the smaller scales of interest here, by contrast, we may regard the VLISM as collisionless.

In the interstellar medium, including the VLISM, galactic cosmic rays are important and contribute to the total energy balance of the plasma. However, galactic cosmic rays are largely excluded from the inner heliosheath (Florinski et al. 2003; Burlaga et al. 2013) and can safely be neglected in the simulations below. In the VLISM in the neighborhood of the heliopause, on kinetic scales, even low energy cosmic rays are completely decoupled from the thermal interstellar plasma—only on scales associated with the diffusive length scale (typically given by the spatial diffusion coefficient κ divided by the characteristic flow speed U i.e., $\kappa/U \sim 10^{24}\ ({\rm m^2\ s^{-1}})/20\ ({\rm km\ s^{-1}}) = 5 \times 10^{20}$ m) do cosmic rays couple dynamically to the background plasma. Consequently, since this scale length far exceeds the fluctuation scales of interest, cosmic rays are irrelevant to the problem at hand. Physical parameters used in the simulation are summarized in Table 1.

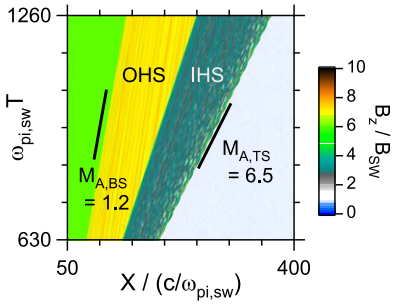

Figure 1. Spatio-temporal evolution of the magnetic field B_z component for Run 1.

3. Simulation Results

3.1. Overview (Run 1)

Figure 1 shows the spatio-temporal evolution of the magnetic field B_z component of Run 1. It is clear that there are four distinct regions separated by three discontinuities. The three discontinuities are, from the right, a forward shock, a contact discontinuity, and a reverse shock, in the context of the shock tube problem. They correspond to the termination shock (TS) for the SW, the heliopause (HP), and the bow shock (BS) in IS space, respectively. The four distinct regions from the right correspond to the unshocked SW, the shocked SW/inner heliosheath (IHS), the shocked IS plasma/outer heliosheath (OHS), and the unshocked IS plasma, respectively. From the slope associated with a discontinuity, the Alfvén Mach number of the TS is estimated as $M_{A,TS} \approx 6.5$ and that of the BS as $M_{A,BS} \approx 1.2$. If one assumes time stationarity of each shock, these values and the values of upstream plasma beta and shock angle with specific heat ratio $\gamma = 2$ yields a theoretical compression ratio of the two shocks as 2.8 and 1.2, respectively.

Figure 2 denotes, from the top, profiles at $\omega_{pi,SW}T = 1260$ of the (a) magnetic field B_y component, (b) B_z component, (c) electron density N_e, (d) phase space density of all ions, (e) IS ions, (f) SW ions, (g) that of all electrons, (h) IS electrons, and (i) SW electrons, respectively. The three discontinuities are again clearly seen in all the panels except for panel (a) which is the incompressible magnetic field component that does not appear in the exactly perpendicular geometry case ($\Theta_{Bn,IS} = \Theta_{Bn,SW} = 90°$). The horizontal dashed lines in panel (c) denote the values of the density inferred from the Rankine–Hugoniot relations as mentioned above. From panels (d)–(i), it is confirmed that the IS plasma and the SW plasma are clearly separated at the HP, although a small fraction of both ion species can be found roughly within a distance of a typical ion gyro radius. While in the oblique cases (Runs 2–5) some particles propagate across the HP along the magnetic field lines, the basic features above continue to hold.

It is notable that fluctuations in density as well as the magnetic field B_z component are apparent in both the IHS and the OHS (see Figures 1 and 2). The origin of the fluctuations will be discussed later.

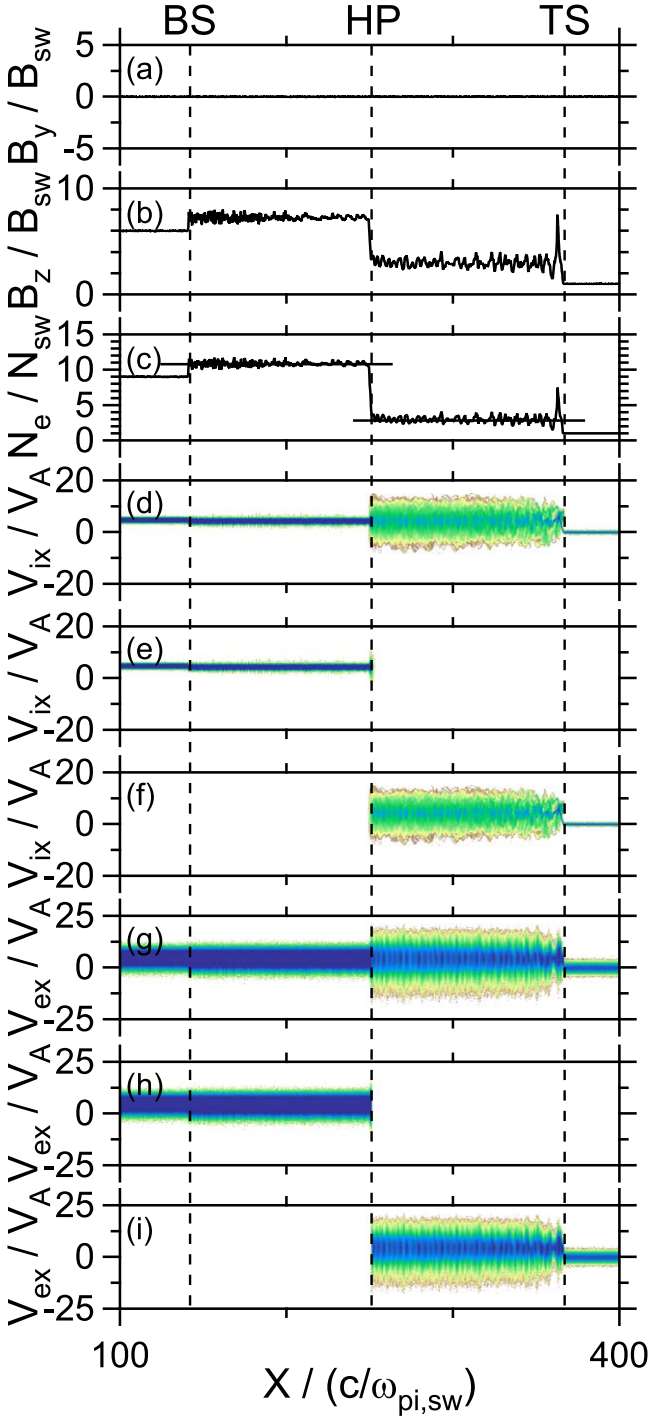

Figure 2. Field profiles and phase space densities at $\omega_{pi,sw}T = 1260$ for Run 1. From the top, magnetic field (a) B_y, (b) B_z, (c) electron density N_e, phase space density of (d) all ions, (e) IS ions, (f) SW ions, (g) all electrons, (h) IS electrons, and (i) SW electrons, respectively, are plotted. The horizontal dashed lines in (c) denote the downstream densities of the two shocks inferred from the Rankine–Hugoniot relations.

3.2. Structure of Contact Discontinuity

3.2.1. Spatial Scale

The dependence of the spatial scale of the contact discontinuity (HP) with Θ_{Bn} is examined here. Figure 3 shows the widths of the HP, L_{HP}, at $\omega_{pi,sw}T = 1260$ for all the runs. The width is defined as the distance between the two points at which the density deviates from its averaged shock downstream value by $1N_{e,SW}$. In an oblique geometry ($\Theta_{Bn,IS} < 90°$), particles can cross the HP as they move along a magnetic field line. This results in mixing of the IS plasma and the SW plasma near the HP, as seen in Figure 4 for Run 3, and makes the width of the HP larger than that of the perpendicular case (Run 1).

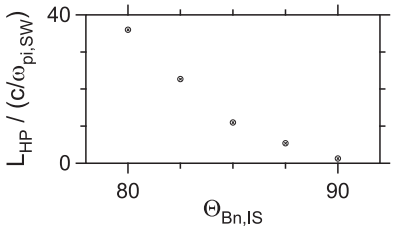

Figure 3. Spatial width of the contact discontinuity as a function of magnetic field obliquity $\Theta_{Bn,IS}$ with respect to IS plasma.

The mixing region expands as the magnetic field becomes more oblique.

Note that when $\Theta_{Bn} < 90°$, B_z should be conserved across the HP if the HP is a contact discontinuity. However, this is not true in the runs 2–5 (e.g., Figure 4(b)). Indeed, we confirmed that the transverse momentum is not conserved across the HP in these runs. Therefore, the HP here is no longer a contact discontinuity formally. This may indicate that the system has not yet reached a steady state. However, we assume that the following features hold in the actual HP.

3.2.2. Inner Structure

The deviation of the spatial profiles between the magnetic field and density in the HP becomes significant when Θ_{Bn} becomes smaller. In particular, a clear hump appears only in the density when $\Theta_{Bn,IS} = 80°$ (Run 5) as shown in Figure 5 and $\Theta_{Bn,IS} = 82.5$ (Run 4: not shown). The detailed structure near the hump in the region indicated by the arrow in Figure 5, is illustrated in Figure 6. In the density hump, between the two vertical lines, the parallel pressure of the ions (and electrons) dominates the total pressure. This region coincides with the region where SW ions and IS ions overlap in phase space, as shown in the fifth panel. These two ion populations interpenetrate as they move along the magnetic field. As a result, the local density is enhanced. Furthermore, the two populations are well separated in the V_z–X phase space so that the local pressure is effectively well enhanced along the magnetic field direction. The electrons basically follow the ions and show a similar feature, while their effective parallel pressure is enhanced even deeper in the OHS where part of the hotter IHS electrons penetrate further. Note that this structure is a non-MHD effect.

3.3. Fluctuations Downstream of Shocks

The downstream region of the two shocks is turbulent in all the runs. This is clearly confirmed, for instance, in Figures 7 and 8 showing the spatio-temporal evolution of B_y, B_z, and N_e in Run 3 and Run 5, respectively. The IHS contains fluctuations of all three components, while the OHS contains fluctuations of only two components, B_z and N_e. This is true for Run 2 to Run 5.

3.3.1. Fluctuations in IHS

One possible source of the fluctuations in the IHS is the temperature anisotropy. An ion temperature anisotropy may drive instabilities such as the Alfvén ion cyclotron (AIC) instability or an electromagnetic ion cyclotron instability and mirror instability. In Run 1 the ion temperature perpendicular to the magnetic field is roughly 20 times higher than that parallel to the magnetic field in the IHS ($T_{i\perp,IHS}/T_{i\parallel,IHS} \sim 20$). Using

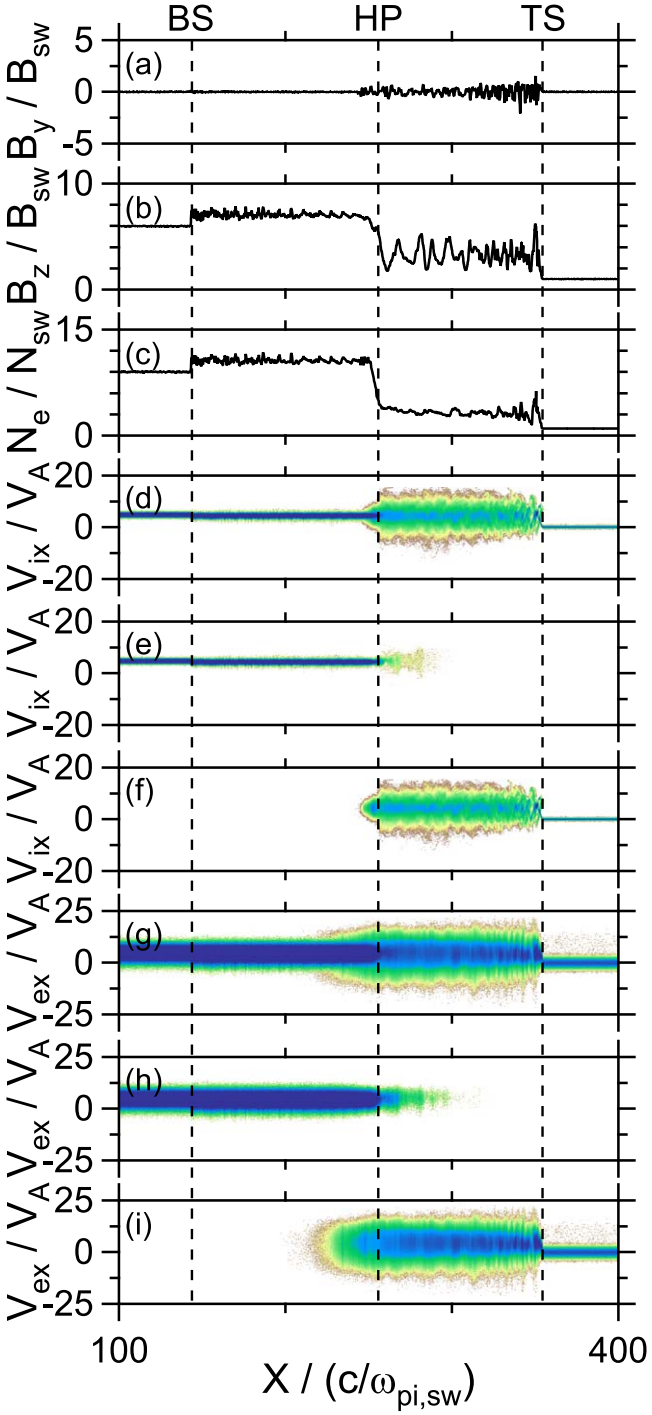

Figure 4. Field profiles and phase space densities at $\omega_{pi,sw}T = 1260$ for Run 3 (same format as Figure 2).

this value and other parameters in the IHS estimated from the simulation, the growth rate of the instabilities are calculated numerically by solving the linear dispersion relation for a bi-Maxwellian hot plasma as shown in Figure 9. Here, the ratio of local electron plasma frequency to cyclotron frequency is fixed as $\omega_{pe,IHS}/\Omega_{e,IHS} = 4$ for simplicity. (We confirmed that the dependence on this ratio is rather small.) The solid lines denote the linear growth rate of the mirror instability for various wave propagation angles with respect to magnetic field, θ_{Bk}. The values of θ_{Bk} correspond roughly to those in the IHS for Run 2 ($\theta_{Bk} = 85°$) and to Run 5 ($\theta_{Bk} = 70°$). The dashed line

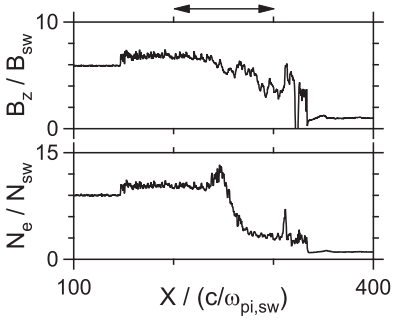

Figure 5. Spatial profiles of B_z and N_e for Run 5.

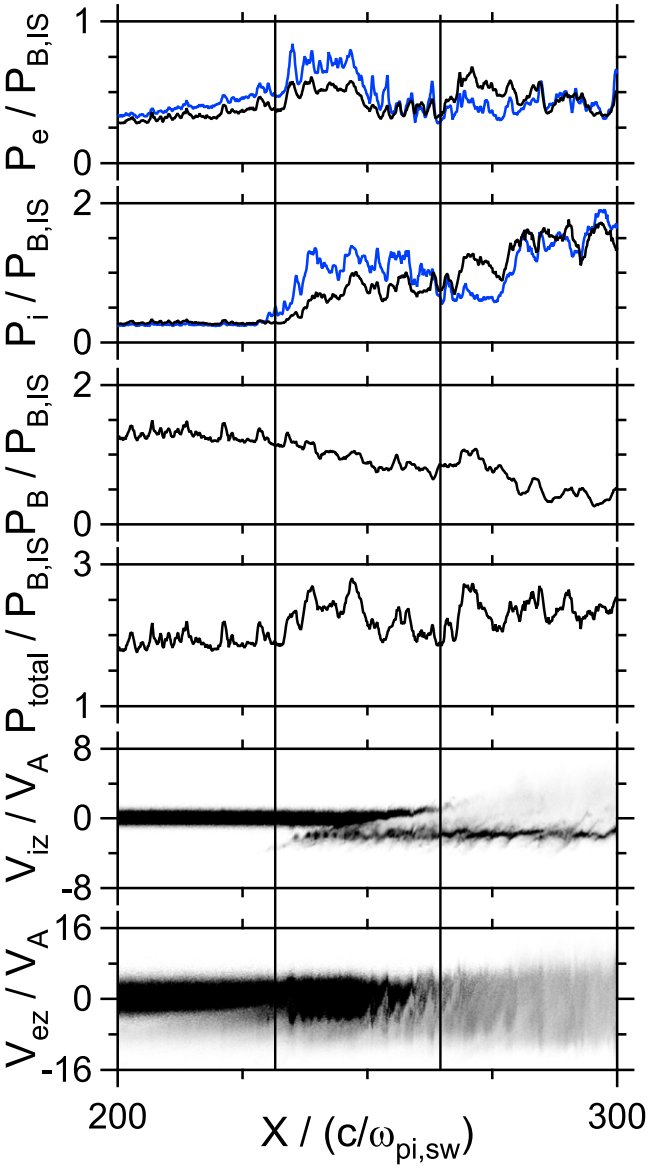

Figure 6. Expanded view of the structure near the HP for Run 5. From the top, electron pressure parallel (blue) and perpendicular (black) to the magnetic field, ion pressure parallel (blue) and perpendicular (black) to the magnetic field, magnetic pressure, total pressure, ion phase space density in V_z–X, and electron phase space density in V_z–X, respectively. The density hump in Figure 5 corresponds to the region between the two vertical lines.

indicates the linear growth rate of the AIC instability at $\theta_{Bk} = 70°$ (Run 5). The growth rate of this instability is too small or even negative when $\theta_{Bk} \geqslant 75°$. By comparing this

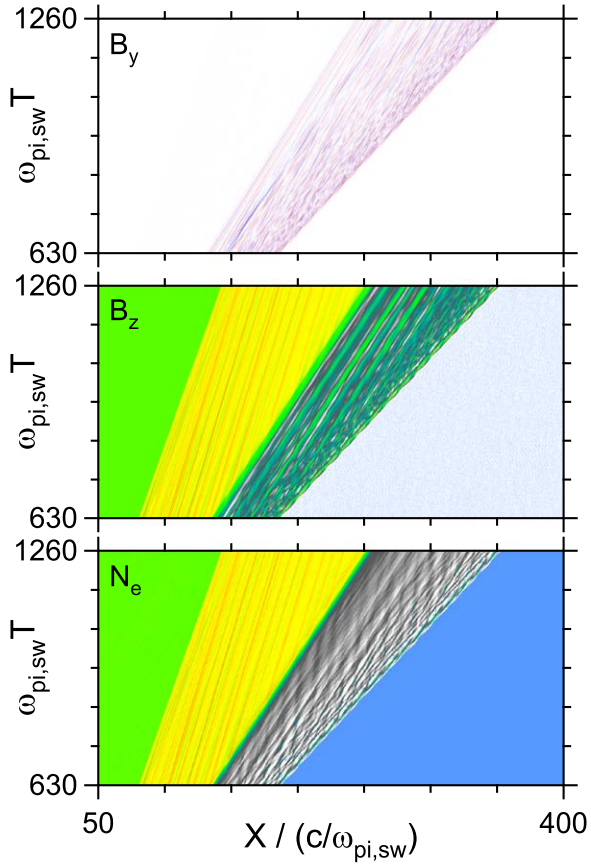

Figure 7. Spatio-temporal evolution of the incompressible (B_y) and compressible (B_z) magnetic fields, and electron density (N_e) for Run 3.

linear analysis with Figures 7 and 8, we conclude that the apparent wavy structures that are phase standing with respect to the HP seen in B_z of Figures 7 and 8 are due to the mirror instability.

Self-reformation of the surface of TS is another source of IHS fluctuations in this particular simulation. Since the TS is a fast mode shock, the reformation leads to in-phase oscillations between B_z and N_e (N_i). This type of oscillation is present in all the runs (e.g., Figure 8) and they have amplitudes as large as the waves generated by the linear instabilities discussed above. Such large amplitude waves can further be sources of other waves through nonlinear processes, like wave–wave couplings, which are not discussed in this paper. As a result, the IHS in each run contains a variety of wave modes, fast, slow, intermediate, and mirror modes, propagating in both positive and negative directions.

Besides the above, there are undoubtedly other causes of fluctuations in the actual IHS. Disturbances in the SW can be a dominant source of the fluctuations in IHS (Donohue & Zank 1993; Story & Zank 1997; Zank & Mueller 2003; Washimi et al. 2011). Turbulent magnetic reconnection occurring in the IHS is another possible source. Regardless of the source of the fluctuations, we discuss the possibility that the fluctuations in the IHS are transmitted through the HP into the OHS.

3.3.2. *Fluctuations in the OHS*

In Figures 7 and 8 fluctuations in the OHS are visible in B_z and N_e, while B_y exhibits no signal in the same region. Here, B_y

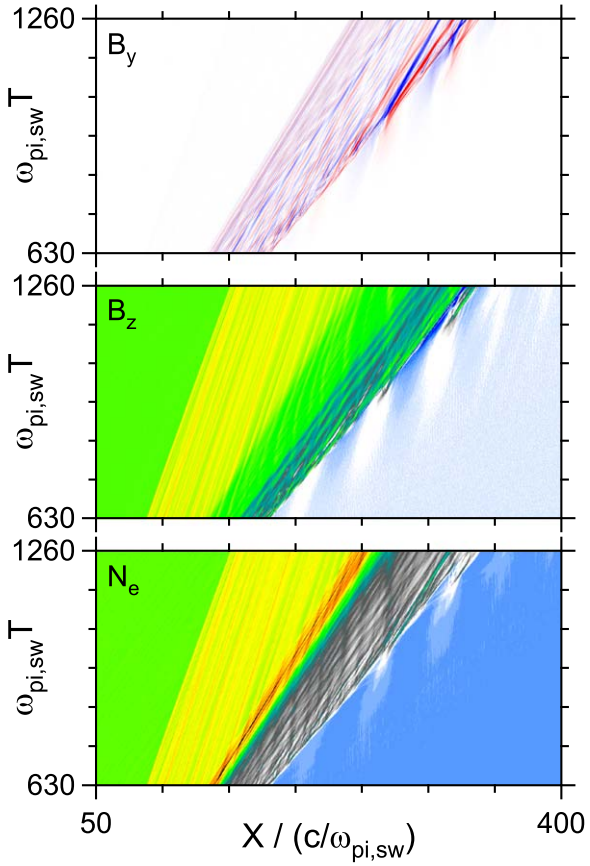

Figure 8. Spatio-temporal evolution of the incompressible (B_y) and compressible (B_z) magnetic fields, and electron density (N_e) for Run 5.

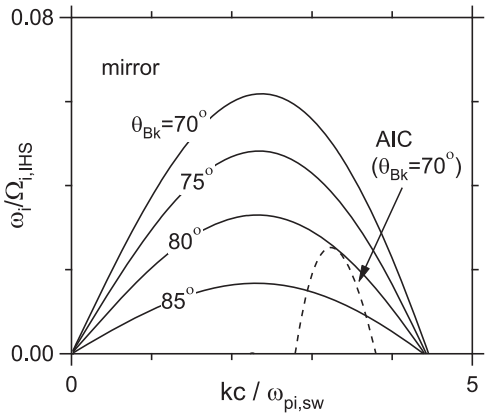

Figure 9. Linear growth rate of instabilities driven by ion temperature anisotropy in the IHS. The solid lines indicate the mirror instability for various wave propagation angles. The dashed line denotes the AIC instability. See the text for details.

indicates the incompressible component of the magnetic fluctuations. Clearly, the incompressible fluctuations produced in the IHS are confined in the same region and are not transmitted to the OHS. On the other hand, the OHS fluctuations in B_z and N_e, which are compressible components, clearly propagate away from the HP.

Figure 10 is an expansion of the middle panels (B_z) of Figures 7 (Run 3) and 8 (Run 5). The horizontal axis denotes the relative distance from the HP. It is clear that the wave peaks in the OHS ($X < X_{HP}$) are continuously linked with those in the

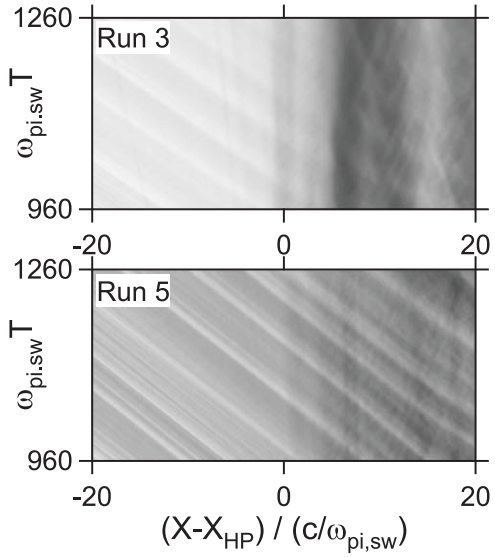

Figure 10. Details of wave propagation near the HP for Run 3 (upper panel) and Run 5 (lower panel). In both panels the gray scale denotes the magnitude of B_z. The horizontal axis is the relative distance from the HP and the vertical axis is time.

IHS ($X > X_{HP}$), indicating that the waves originated in the IHS, although other waves are also present in the IHS.

The correlation between the magnetic and density fluctuations in the IHS and OHS for different runs is shown in Figure 11 as a scatter plot of density versus magnetic fluctuations. It shows a clear positive correlation between them in the OHS as seen in the left panels, even when the two components do not have clear positive correlations in the IHS (right panels). This indicates that among the compressible waves generated in the IHS, only the fast mode waves can pass the HP into the OHS in the present simulations.

3.3.3. Effect of the HP

Figure 12 denotes the ω–k spectra of B_z in the OHS in Run 3 (upper panel) and Run 5 (middle panel), and in the IHS in Run 5 (bottom panel) in the frame moving with the HP. In the OHS the dominant peak appears in the second quadrant. This is consistent with the OHS fluctuations propagating away from the HP in Figures 7 and 8. The black dashed lines in both (upper and middle) panels show the local Alfvén velocity, which is close to the phase velocity of local fast mode waves, since the local plasma in the OHS has a low plasma beta. In the IHS the dominant peak again appears in the second quadrant slightly above the black dashed line indicating the local Alfvén velocity, while other wave modes can also be recognized in the first and second quadrants. The difference between the bottom two panels again indicates that only the fast mode waves existing in the IHS can cross the HP into the OHS (VLISM).

This scenario indeed is theoretically and numerically supported. Zank et al. (2017) show that the conditions at the heliospheric boundary region allow only fast mode waves in the IHS to cross the HP by considering the so-called Snell's law. It is also shown by Washimi et al. (2007, 2011, 2017) using their MHD simulation that large amplitude fast mode disturbances in the SW are partially transmitted through the HP. However, the simulation result here appears to show a discrepancy from the theory based on Snell's law. Although in theory, the wave frequency should not change across the HP,

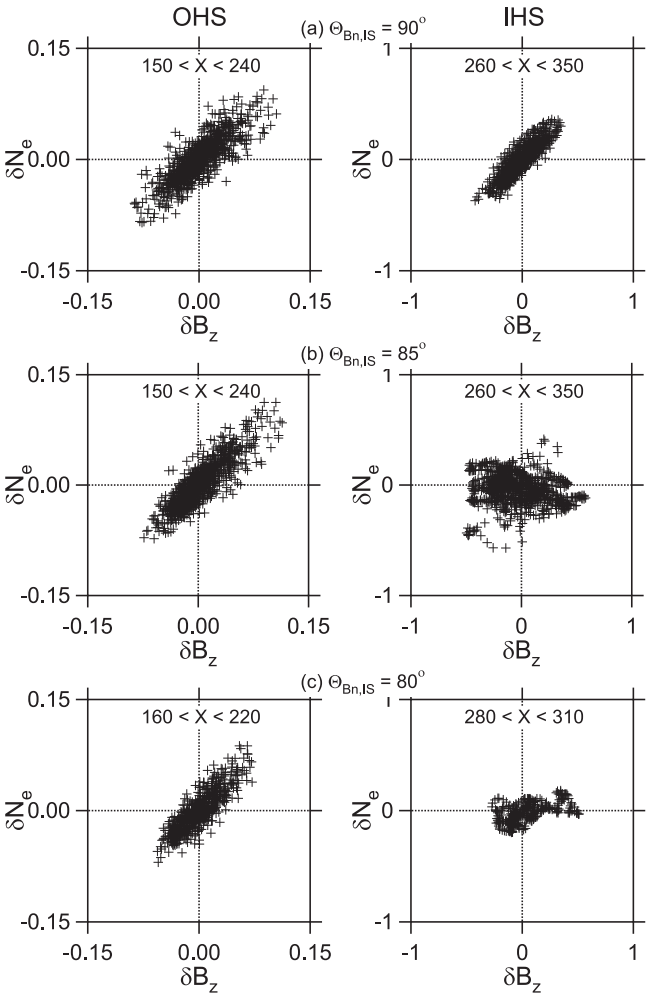

Figure 11. Scatter plots between density (δN_e) and compressible magnetic (δB_z) fluctuations in the OHS (left panels) and the IHS (right panels) for (a) Run 1, (b) Run 3, and (c) Run 5.

the frequency of the fast mode waves increases after crossing the HP. One possible explanation for this is wave steepening. Figures 13(a) and (c) denote the expanded view of B_z near the HP for Run 3 and Run 5, respectively. The waveforms in $X < X_{\rm HP}$ is clearly steepened, although no steepened feature is seen in $X > X_{\rm HP}$. This is confirmed more clearly in (b) and (d) where the fluctuations having wavelengths of $4.3c/\omega_{\rm pi,sw}$ or longer are filtered out from (a) and (c), respectively. The fast mode waves generated in the IHS are steepened when crossing the HP. This may result in broadening the wave spectrum in the OHS.

4. Summary and Discussions

In this study one-dimensional PIC simulations were performed to investigate the so-called shock tube problem in a collisionless plasma in which a relatively tenuous and weakly magnetized plasma is continuously pushed by a relatively dense and strongly magnetized plasma having supersonic relative velocity. The structure of the boundary region includes three discontinuities, forward and reverse shocks and a contact discontinuity. The spatial width of the contact discontinuity increases as $\Theta_{\rm Bn}$ decreases. The spatial profiles of the magnetic field and plasma density, or pressure, of the contact discontinuity change significantly when $\Theta_{\rm Bn,IS}$ deviates from 90°. This is a non-MHD or kinetic effect of

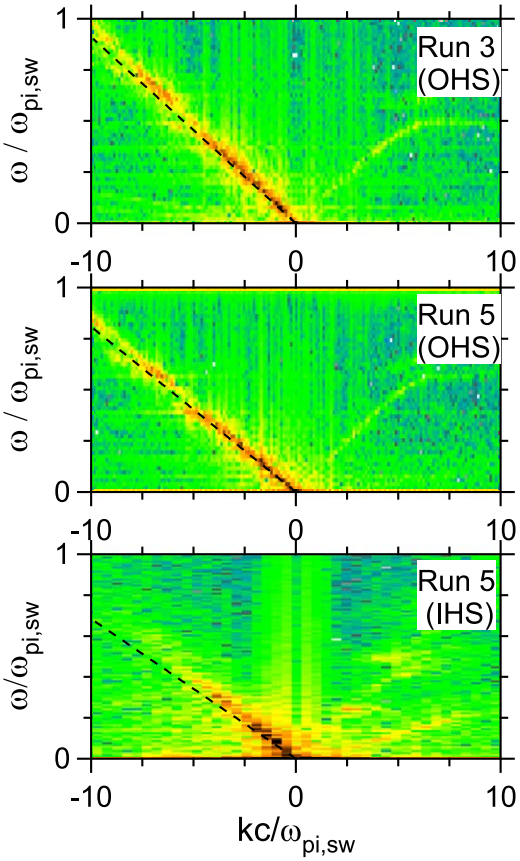

Figure 12. ω–k spectra of B_z for Run 3 (upper panel) and Run 5 (middle and bottom panels). The corresponding time interval is $941 \leqslant \omega_{\rm pi,sw}T \leqslant 1265$. The spatial region is $-56.87 \leqslant (X - X_{\rm HP})/(c/\omega_{\rm pi,sw}) \leqslant -5.06$ for the upper and the middle panels, while $5.06 \leqslant (X - X_{\rm HP})/(c/\omega_{\rm pi,sw}) \leqslant 56.87$ for the bottom panel.

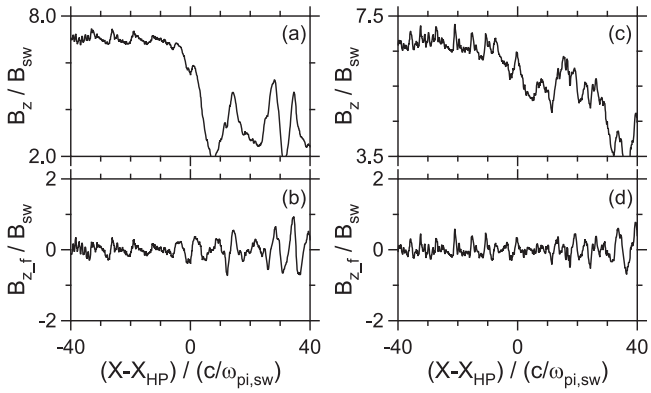

Figure 13. Expanded view of B_z near the HP for (a) Run 3 and (c) Run 5. The panels (b) and (d) are obtained from (a) and (c), respectively, by applying a high pass filter where fluctuations of wavelength $4.3c/\omega_{\rm pi,sw}$ or larger are filtered out.

the local plasma that allows charged particles to stream across the contact discontinuity. Many kinds of magnetic and density fluctuations are observed in the region between the two shocks. Among them, the fluctuations between the reverse shock and the contact discontinuity (OHS) are fast magnetosonic modes and propagate away from the contact discontinuity. Their origin is on the IHS side of the contact discontinuity.

If we regard the above boundary structures as mimicing the heliospheric boundary, the forward and the reverse shocks

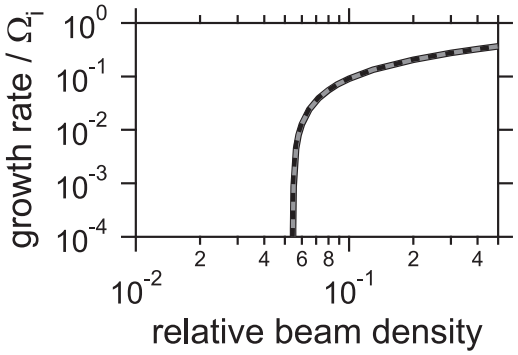

Figure 14. Linear growth rate of the right-hand resonant ion beam instability that may occur in the density hump. For further details, see the text.

correspond to the SW termination shock and the bow shock, and the contact discontinuity to the heliopause, respectively. In the context of heliospheric physics the TS is a reverse shock and the BS, if present, is a forward shock.

A difference in the profiles between the magnetic field and cosmic-ray count rate at the heliopause is observed by *Voyager 1* (Burlaga & Ness 2014). This indicates that the observed cosmic rays are not tied to the local magnetic field within the scale of the changing magnetic field. This is consistent with our simulation result that even the background plasma does not satisfy the frozen-in condition locally in the heliopause. From the simulation, the plasma density or pressure is more enhanced than the magnetic field in the heliopause. This discrepancy between the plasma and the magnetic field profiles may be sustained unless the separation between the SW plasma and the IS plasma in the local phase space is relaxed. Such relaxation may occur through either collisionless or collisional processes. Mostafavi & Zank (2018) showed that collisional mean free paths of various kinds (p–p, e–p) in the VLISM are typically of the order of 0.1 au. On the other hand, collisionless instabilities may occur through ion–ion two stream interactions. According to Richardson et al. (2018), plasma parameters observed by *Voyager 2* in the IHS after 2018 are typically $N \sim 2 \times 10^{-3}$ cm^{-3}, $T \sim 5$ eV, and $|V| \sim 10^2$ km s^{-1}, respectively. Here, N is the density, T the thermal proton temperature, and $|V|$ denotes the bulk flow speed. The typical magnetic field strength also observed by *Voyager 2* in the IHS in 2015 is of the order of 0.1 nT (Burlaga et al. 2018b), which is consistent with *Voyager 1* observations in the IHS (Burlaga et al. 2014). From these values, the local Alfvén velocity is estimated as $V_A \sim 50$ km s^{-1}. In the OHS or VLISM, the magnetic field and thermal plasma density increase, although an exact value of the latter is not yet well known. If the two plasmas interpenetrate in the heliopause transition region as seen in the simulation, the right-hand resonant instability may possibly be generated. By way of illustration, we calculated the linear growth rate of the instability as a function of relative beam density, which is defined as the SW proton density divided by the IS proton density, for the case that the relative bulk velocity of the two warm proton beams is $2V_A$ (Figure 14). The temperature of the SW protons is assumed to be 5 eV, while that of the IS protons is taken to be 1 eV (black solid line) and 25 eV (gray solid line although almost hidden by the black solid line). We also assume that there are two nonthermal populations. One is PUIs whose relative density is 25% and temperature is 100 eV. Another nonthermal population is assumed to be present and to have a much lower relative density, 1%, and much higher temperature such as 10 keV (black and gray solid lines) and 1 MeV (black dashed line). This component might be related to anomalous or galactic cosmic rays for example. We find that the resultant growth rates of the instability do not much depend on the above temperature variations and that the growth rate becomes of the order of $10^{-2}\Omega_i$ or larger when the relative beam density reaches roughly 6%. Here, Ω_i denotes proton cyclotron frequency. The local magnetic field is several times larger than 0.1 nT (Burlaga & Ness 2014) so that the corresponding timescale of the wave growth is a few thousand seconds. During this time, the plasma, having a typical bulk flow speed of 100 km s^{-1}, travels roughly $\sim 10^5$ km ($10^{-2} \sim 10^{-3}$ au) which is much less than the collisional mean free path. As illustrated in Figure 14, the growth rate of the instability is even higher for larger relative beam densities so that the above effective mean free path may have been overestimated. Another known non-MHD structure in boundary regions is the plasma depletion layer (PDL), which is observed in front of planetary magnetopauses and thought to exist beyond the HP (Fuselier & Cairns 2013; Cairns & Fuselier 2017). The spatial scale of the PDL along the trajectory of *Voyager 1* is estimated as 2.6 au from the Plasma Wave Subsystem as well as the Magnetometer instrument data on board *Voyager 1*. Therefore, the density hump discussed here has a quite different spatial scale from the PDL.

Burlaga et al. (2018a) showed that magnetic turbulence in the VLISM observed by *Voyager 1* during an interval from 2013.3593 to 2014.6373 is more or less compressible. During that time *Voyager 1* was rather close to the heliopause. Possible sources of the compressible fluctuations are discussed by Burlaga et al. (2018a). A bow shock (or a bow wave) is one possibility. However, the bow shock is expected to be very weak, even if it exists (McComas et al. 2012; Zank et al. 2013). Although our simulation reproduced a weak reverse shock, dominant fluctuations do not propagate from the reverse shock but do propagate toward it. Hence, a bow shock is unlikely to be a source of the observed turbulence as long as it is very weak. A second possibility raised by Burlaga et al. (2018a) is that the turbulence is generated in the OHS or VLISM. Furthermore, they mention that the heliopause itself can also be a source. These possibilities are not negated from our simulations. The fourth possibility is that the fluctuations might originate in the IHS and pass through the heliopause into the OHS or VLISM, which is suggested by Burlaga et al. (2015) and theoretically demonstrated by Zank et al. (2017). Our simulation here supports this scenario. The heliopause works as a filter at which incompressible fluctuations and compressible slow mode fluctuations present in the IHS are filtered out, and only the compressible fast mode fluctuations can pass through it. This is what was expected theoretically by Zank et al. (2017). In our simulation it is also shown that the wave spectrum in the OHS or VLISM is broadened. A possible explanation for this is the wave steepening, i.e., the fast mode fluctuations generated in the IHS are steepened when passing the HP. Another possible explanation may be based on the inhomogeneous flow velocity around the HP. When the mean flow velocity changes, which is actually confirmed in Run 5 ($\Theta_{Bn,IS} = 80°$), the wave frequency can change as a result of the conservation of wave action (Bretherton & Garrett 1968; Zank & McKenzie 1987).

The simulation here is one-dimensional. All higher dimensional structures and phenomena in the boundary region are ignored. Also only the main population of the SW has been taken into account. Furthermore, some parameters used in the simulations are not realistic. We comment briefly on these points below. On the kinetic scales of the problem, the scale of curvature of a heliopause located at 124 au or so is essentially

zero, i.e., as far as the kinetic scale waves are concerned, the heliopause is a planar structure. Thus we neglect the fact that the streamline of the plasma near the heliopause gradually bends along its surface. The relative tangential flow speeds across the heliopause are not especially large and would result primarily in a Doppler-shift in the frequency without significantly modifying the physics of the problem (we are not considering a Kelvin–Helmholtz instability—see, for example, the discussion in Avinash et al. 2014 related to this point). Moreover, some important effects in the heliospheric boundary region, like charge exchange and pickup ion dynamics, are also not taken into account. As discussed above, charge exchange can be neglected in the simulation. However, we believe that the presence of distinct nonthermal populations do not significantly alter the essential wave properties observed in the current simulations. The shock jump conditions determine the correct total thermal and kinetic energy in the inner heliosheath, regardless of whether the nonthermal populations are included explicitly or not. Nonetheless, it is fair to say that the distribution is not a thermal equilibrium Maxwellian distribution. Immediately downstream of the termination shock, both the thermal ions and the pickup ions exhibit temperature anisotropies (Matsukiyo et al. 2007). Zank et al. (2010) showed that the inner heliosheath distribution can be approximated rather well by an isotropic kappa distribution. The distribution function in the inner heliosheath that we compute does depart from a simple Maxwellian because of dissipative processes (ion reflection) at the heliospheric termination shock. In this regard, it probably captures somewhat reasonably the more complicated distribution function expected in the inner heliosheath (certainly better than can be expected from a 3D MHD-neutral H model). Furthermore, some parameters such as the mass ratio and frequency ratio ($\omega_{\mathrm{pe,SW}}/\Omega_{e,\mathrm{SW}}$) are far from the realistic values. It is known that changing these parameters may result in a change of wave generation mechanisms. For example, a number of instabilities excited in the transition region of a collisionless shock show different parameter dependences (Wu et al. 1984). For this reason, we have not focused on the generation mechanism for waves seen in the region downstream of the termination shock in this paper. However, regardless of their generation mechanisms, we believe that the wave propagation properties across the HP discussed in this paper are correct at least qualitatively.

This work was supported by Grant-in-Aid for Scientific Research (C) No. 19K03953 from JSPS (S.M.). G.P.Z. acknowledges partial support by an *IBEX* subaward SUB 0000167/NASA 80NSSC18k0237 and a NSF EPSCoR RII-Track-1 Cooperative Agreement OIA-1655280.

ORCID iDs

S. Matsukiyo https://orcid.org/0000-0002-4784-0301
G. P. Zank https://orcid.org/0000-0002-4642-6192

References

Avinash, K., Zank, G. P., Dasgupta, B., & Bhandoria, S. 2014, ApJ, 791, 102
Bretherton, F. P., & Garrett, C. J. R. 1968, RSPSA, 302, 529
Burgess, D., Gingell, P. W., & Matteini, L. 2016, ApJ, 822, 38
Burlaga, L. F., Florinski, V., & Ness, N. F. 2015, ApJL, 804, L31
Burlaga, L. F., Florinski, V., & Ness, N. F. 2018a, ApJ, 854, 20
Burlaga, L. F., & Ness, N. F. 2014, ApJ, 784, 146
Burlaga, L. F., Ness, N. F., Acuna, M. H., et al. 2005, Sci, 309, 2027
Burlaga, L. F., Ness, N. F., Acuna, M. H., et al. 2008, Natur, 454, 75
Burlaga, L. F., Ness, N. F., Florinski, V., & Heerikhuisen, J. 2014, ApJ, 792, 134
Burlaga, L. F., Ness, N. F., & Stone, E. C. 2013, Sci, 341, 147
Burlaga, V., Ness, N. F., & Richardson, J. D. 2018b, ApJ, 861, 9
Cairns, I. H., & Fuselier, S. A. 2017, ApJ, 834, 197
Decker, R. B., Krimigis, S. M., Roelof, E. C., et al. 2005, Sci, 309, 2020
Decker, R. B., Krimigis, S. M., Roelof, E. C., et al. 2008, Natur, 454, 67
Donohue, D. J., & Zank, G. P. 1993, JGR, 98, 19005
Drake, J. F., Swisdak, M., Opher, M., & Richardson, J. D. 2017, ApJ, 837, 159
Florinski, V., Heerikhuisen, J., Niemiec, J., & Ernst, A. 2016, ApJ, 826, 197
Florinski, V., Zank, G. P., Heerikhuisen, J., Hu, Q., & Khazanov, I. 2010, ApJ, 719, 1097
Florinski, V., Zank, G. P., & Pogorelov, N. V. 2003, JGRA, 108, 1228
Fuselier, S. A., & Cairns, I. H. 2013, ApJ, 771, 83
Giacalone, J., & Burgess, D. 2010, GeoRL, 37, L19104
Giacalone, J., & Decker, R. 2010, ApJ, 710, 91
Gurnett, D. A., & Kurth, W. S. 2005, Sci, 309, 2025
Gurnett, D. A., & Kurth, W. S. 2008, Natur, 454, 78
Gurnett, D. A., Kurth, W. S., Burlaga, L. F., & Ness, N. F. 2013, Sci, 341, 1489
Krimigis, S. M., Decker, R. B., Roelof, E. C., et al. 2013, Sci, 341, 144
Kucharek, H., & Scholer, M. 1995, JGR, 100, 1745
Lee, R. E., Chapman, S. C., & Dendy, R. O. 2005, AnGeo, 23, 643
Lembege, B., & Yang, Z. 2018, ApJ, 860, 84
Liewer, P. C., & Goldstein, B. E. 1993, JGR, 98, 15211
Liewer, P. C., Sharadini, R., & Goldstein, B. E. 1995, JGR, 100, 19809
Lipatov, A. S., & Zank, G. P. 1999, PhRvL, 82, 3609
Lipatov, A. S., Zank, G. P., & Pauls, H. L. 1998, JGR, 103, 29679
Liu, K., Gary, S. P., & Winske, D. 2010, JGR, 115, A12114
Liu, K., Moebius, E., Gary, S. P., & Winske, D. 2012, JGR, 117, A10102
Matsukiyo, S., & Scholer, M. 2011, JGR, 116, A08106
Matsukiyo, S., & Scholer, M. 2014, JGRA, 119, 2388
Matsukiyo, S., Scholer, M., & Burgess, D. 2007, AnGeo, 25, 283
McComas, D. J., Alexashov, D., Bzowski, M., et al. 2012, Sci, 336, 1291
Min, K., & Liu, K. 2018, ApJ, 852, 39
Mostafavi, P., & Zank, G. P. 2018, ApJL, 854, L15
Niemiec, J., Florinski, V., Heerikhuisen, J., & Nishikawa, K.-I. 2016, ApJ, 826, 198
Oka, M., Zank, G. P., Burrows, R. H., & Shinohara, I. 2011, in AIP Conf. Proc. 1366, PARTIALLY IONIZED PLASMAS THROUGHOUT THE COSMOS —PROCEEDINGS OF THE 2010 HUNTSVILLE WORKSHOP, ed. V. Florinski (Melville, NY: AIP), 53
Richardson, J. D., Belcher, J. W., Cummings, A. C., Decker, R., & Stone, E. C. 2018, JPhCS, 1100, 012019
Richardson, J. D., Kasper, J. C., Wang, C., Belcher, J. W., & Lazarus, A. J. 2008, Natur, 454, 63
Stone, E. C., Cummings, A. C., McDonald, F. B., et al. 2005, Sci, 309, 2017
Stone, E. C., Cummings, A. C., McDonald, F. B., et al. 2008, Natur, 454, 71
Stone, E. C., Cummings, A. C., McDonald, F. B., et al. 2013, Sci, 341, 150
Story, T. R., & Zank, G. P. 1997, JGR, 102, 17381
Washimi, H., Tanaka, T., & Zank, G. P. 2017, ApJL, 846, L9
Washimi, H., Zank, G. P., Hu, Q., et al. 2011, MNRAS, 416, 1475
Washimi, H., Zank, G. P., Hu, Q., Tanaka, T., & Munakata, K. 2007, ApJL, 670, L139
Wu, C. S., Winske, D., Zhou, Y. M., et al. 1984, SSRv, 37, 63
Wu, P., Liu, K., Winske, D., et al. 2010, JGR, 115, A11105
Wu, P., Winske, D., Gary, S. P., Schwadron, N. A., & Lee, M. A. 2009, JGR, 114, A08103
Yang, Z., Liu, Y. D., Richardson, J. D., et al. 2015, ApJ, 809, 28
Zank, G. P., Du, S., & Hunana, P. 2017, ApJ, 842, 114
Zank, G. P., Heerikhuisen, J., Pogorelov, N. V., Burrows, R., & McComas, D. J. 2010, ApJ, 708, 1092
Zank, G. P., Heerikhuisen, J., Wood, B. E., et al. 2013, ApJ, 763, 20
Zank, G. P., & McKenzie, J. F. 1987, JPlPh, 37, 347
Zank, G. P., & Mueller, H.-R. 2003, JGRA, 108, 1240